



Collaboration of Ni, polyoxometalates and layered double hydroxides: synthesis, characterization, electrochemical and mechanism investigations as nano-catalyst in the Heck coupling reaction

Ezzat Rafiee^{1,2} · Masoud Kahrizi¹

Received: 3 May 2018 / Accepted: 9 August 2018
© Springer Nature B.V. 2018

Abstract

Nickel (Ni) nanoparticles were immobilized on the surface of magnetic MgAl layered double hydroxide intercalated 10-molybdo-2-vanadophosphate (Fe–MgAl/Mo₁₀V₂–Ni) for the first time. The presence of Ni nanoparticles on the high-surface area Fe–MgAl LDH structure in the presence of Mo₁₀V₂ makes this catalyst an ideal option in terms of efficiency and selectivity for Heck coupling reaction. Synergic effects of Mo₁₀V₂ and Ni were investigated by an electrochemical technique. Increasing of the ECSA of the catalyst compared to Fe–Mg–Al–Ni leads to enhancement of the catalytic activity and proves the synergic effect. A new catalytic mechanism was introduced for this kind of reaction. The resulting structure and its catalytic behavior were characterized by FT-IR, XRD, ICP-AES, TEM, SEM, EDX, EBSD, XPS, BET, VSM, CV, LSV and zeta potential analyses. More importantly, Fe–MgAl/Mo₁₀V₂–Ni can easily be separated from the reaction mixture using an external magnet and reused for at least four successive runs without any substantial reduction in its catalytic activity.

Keywords Polyoxometalate · Layered double hydroxide · Cyclic voltammetry · Magnetic nano-catalyst · Heck reaction

✉ Ezzat Rafiee
e.rafeei@razi.ac.ir; Ezzat_rafeei@yahoo.com

¹ Faculty of Chemistry, Razi University, Kermanshah 67149, Iran

² Institute of Nano Science and Nano Technology, Razi University, Kermanshah 67149, Iran

Introduction

The palladium (Pd) catalyzed coupling of aryl halides and olefins, known as the Heck reaction is a well-established methodology in modern organic synthesis [1–4]. The coupling products find important applications in different fields of material science such as bioactive compounds, preparation of materials and natural products [5, 6]. Despite the merit of using Pd-based catalysts in the Heck reactions, these types of coupling reactions suffer from major problems, such as using the expensive species as a catalyst, which prevent the industrial development of this catalytic reaction. Also, the use of ligand and base can impose more expense and causes toxicity in these systems.

One of the best ways to address these problems is replacing the Pd-based catalysts by more affordable species. Among the inexpensive transition metals, nickel (Ni) can be an ideal alternative for Pd in the Heck coupling reactions as it is about 500 times cheaper than Pd. Ni also shows faster oxidative addition and more facile olefin insertion compared to Pd [7]. However, the number of attempts to develop a Ni-based catalyst in the Heck coupling reaction are very few [8–10].

Although there are many benefits in the use of Ni catalysts, the homogeneous Ni-based catalysis has significant drawbacks, including environmental pollution, low catalyst stability and possible toxicity caused by residual metal species, which have impeded their large-scale application in industry. To overcome these problems, chemists have investigated the employment of heterogeneous Ni species [11, 12].

Immobilization of Ni nanoparticles on solid structures such as layered double hydroxides (LDHs) can provide many features in the catalytic properties of the catalyst. LDHs are composed of cationic $M(II)_{1-x}M(III)_x(OH)_2^{x+}$ layers which are neutralized with anionic $x/nA^{n-} \cdot zH_2O$ parts [13]. The layers with positive charge include the edge-shared metal M(II) and M(III) hydroxide octahedra, which are accompanied by a negative charge of anions located inside and on the surface of the lamellae. This protocol provides a high-surface area catalyst which directly affects the efficiency and selectivity of LDH-based catalysts [13–17].

A novel approach is putting up the Fe_3O_4 nanoparticles in LDH structures which can be easily recovered from the reaction media using an external magnet. This feature addresses the isolation and recycling problems faced by many catalytic systems. The Fe_3O_4 -LDH system can be formed in a composite-like structure and has been demonstrated to be feasible for catalytic applications [18, 19]. Also, LDHs can provide “flexible” confining spaces that can be adjusted by changing the size and arrangement of guest molecules. The flexible interlayer space can accommodate polyoxometalates (POMs) [20, 21] which can be used as an effective co-catalyst in coupling reactions [22–26].

Nowadays, POMs have found a lot of interest in coupling reactions and growing research has been performed on the use of them in this field of organic reactions [25–28]. POMs with a Brønsted acid property and electron transfer ability can act as a strong activator for reactants and regenerators of the catalyst in the coupling reactions.

Previously, POMs and metal catalysts have been used in separate catalytic structures in carbon–carbon coupling reactions [22, 24, 29]. In continuation of our studies on the development of practical and environmentally friendly procedures for carbon–carbon coupling reactions [22–24, 30], the applicability of a recyclable heterogeneous catalyst, Ni immobilized on an Fe–MgAl LDH structure intercalated with 10-molybdovanado phosphate (Fe–MgAl/Mo₁₀V₂–Ni) for a Heck reaction, was investigated. This catalyst exhibited a remarkable activity and the system tolerates a wide variety of olefin and aryl halide compounds with good to excellent yields of the desired products.

Experimental

General remarks

All the material including reagents and solvents were commercially available and purchased from Fluka, Merck, and Aldrich. A transmission electron microscopy (TEM) analysis was performed using a TEM microscope (Philips CM 120 kV; Netherlands). X-ray diffraction (XRD) patterns were obtained on an Inel French, EQUINOX 3000 model X-ray diffractometer using Cu–K α radiation. Scanning electron microscopy (SEM)/electron backscatter diffraction microscopy (EBSD) was performed using an SU3500 microscope with scanning range from 0 to 20 keV. Electron dispersive X-ray (EDX) measurements were performed with an IXRF model 550i attached to the SEM. SEM-EBSD/EDX samples were prepared by coating solid particles into a conductive layer. Fourier-transform infrared spectroscopy (FT-IR) was recorded with KBr pellets using a Bruker ALPHA FT-IR spectrometer. X-ray photoelectron spectroscopy (XPS) was recorded with a Kratos Analytical Axis Ultra, with monochromatic aluminum and magnesium with an X-ray source of 1.4866 and 1.2536 keV and a concentric hemispherical analyzer (CHA). A take-off angle of 90° was used on a spot size of 700 lm 350 lm. The instrument has an Ultra-High Vacuum. Thermogravimetric analysis (TGA) was carried out using a thermal gravimetric analysis instrument (Shimadzu TA-60WS-TGA-50/50H) with a flow rate of 30 mL min⁻¹ and a heating rate of 10 °C min⁻¹ in air. The magnetic property of Fe–MgAl/Mo₁₀V₂–Ni was measured using a BHV-55 (Riken, Japan) vibrating sample magnetometer. The Ni and Mo contents were measured using inductively coupled plasma atomic emission spectroscopy (ICP-AES) on a Spectro Ciros CCD spectrometer. Zeta potentials were measured with a Nano ZS90 zeta sizer analyzer (Malvern, UK) with 0.001 mol L⁻¹ NaNO₃ electrolyte. The pore volume and specific surface area determination were studied by Brunauer–Emmett–Teller (BET) and Barrett–Joyner–Halenda (BJH) methods, respectively, by use of a Quantachrome Autosorb-1C-VP analyzer. Prior to the measurements, the samples were degassed at 100 °C for 6 h. The electrochemical behavior of the catalyst was measured using a computer-controlled *m*-Autolab modular electrochemical system (SAMA500 ElectroAnalyzer). Thin layer chromatography (TLC) on pre-coated silica gel Fluorescent 254 nm (0.2 mm) on

aluminum plates was used to indicate the reaction progress. The cross-coupling products were characterized by their ^1H NMR spectra [30].

Preparation of Fe_3O_4 nanoparticles

Typically, 4.3 g $\text{FeCl}_2 \cdot 4\text{H}_2\text{O}$ (21.6 mmol) and 11.6 g $\text{FeCl}_3 \cdot 6\text{H}_2\text{O}$ (43.0 mmol) were mixed with 350 mL of deionized water under N_2 atmosphere. The resulting solution was heated to 80 °C while stirring, vigorously. Then, 20 mL of 25% NH_4OH was quickly added to the solution. The resulting dispersion was vigorously stirred for 5 min, and then the black precipitate was collected using a magnet and washed frequently with deionized water and ethanol, then dried under vacuum.

Preparation of Fe–MgAl LDH

Firstly, Fe_3O_4 (0.3 g) was ultrasonically dispersed into 150 mL solvent ($V_{\text{methanol}}/V_{\text{water}} = 1/1$) for 20 min to obtain a uniform dispersion. A 100 mL alkaline solution (0.32 g Na_2CO_3 (3.0 mmol), 0.48 g NaOH (12.0 mmol)) was added dropwise into the dispersion until pH ca. 10.0 and kept for 5 min, then a 100 mL solution of 1.02 g $\text{Mg}(\text{NO}_3)_2 \cdot 6\text{H}_2\text{O}$ (4.0 mmol) and 0.5 g $\text{Al}(\text{NO}_3)_3 \cdot 9\text{H}_2\text{O}$ (1.34 mmol) was added to the previous dispersion and the pH of the above mixture was adjusted to 9.5–10.0. The obtained slurry dispersion was stirred for 5 min followed by separation with an external magnet and washing with deionized water and ethanol, and dried at 60 °C overnight, giving the product Fe–MgAl LDH.

Preparation of Fe–MgAl–Ni

Fe–MgAl–Ni was prepared by the deposition–precipitation procedure as follows. A 255 mL $\text{NiCl}_2 \cdot 6\text{H}_2\text{O}$ aqueous solution (0.008 M) was positioned in an 80 °C water bath. Then, 0.5 g Fe–MgAl LDH was added into this solution under vigorous stirring for 1 h, and the pH of the dispersion was adjusted to 8.0 by 0.1 M NaOH . The resulting slurry was recovered by magnetic separation, followed by washing with deionized water and ethanol, and dried at 60 °C for 24 h to produce Fe–MgAl–Ni.

Preparation of Fe–MgAl/ Mo_{10}V_2 –Ni

Preparation of Fe–MgAl/ Mo_{10}V_2 –Ni was carried out using an anion exchange process. Under N_2 atmosphere, 0.16 g Mo_{10}V_2 (0.092 mmol) was added to 10 mL of an Fe–MgAl–Ni dispersion (0.3 g). The mixture was kept under N_2 and refluxed at 90 °C for 10 h. The resulting solid was filtered and washed with boiling water and hot ethanol three times, and then dried under vacuum.

Electrochemical investigations

The modified carbon paste electrodes (CPE) were prepared by thoroughly mixing powder graphite, Fe–MgAl/ Mo_{10}V_2 –Ni, and paraffin oil until a paste was obtained.

The resulting paste was put into the tip of a micropipette (4 cm long, 0.01 cm diameter) with Cu wire used as an electrical connection. Each time an experiment was performed, the electrode was refreshed by polishing it on a weighing paper. To investigate the electrochemical features of Fe–MgAl/Mo₁₀V₂–Ni, the prepared electrode was inserted into a three-electrode chemical cell composed of a saturated calomel electrode and a platinum counter electrode. All the electrochemical measurements were recorded in a phosphate buffer solution of pH = 7 (PBS) as a supporting electrolyte and under different scan rates.

General procedure for the Heck coupling reaction

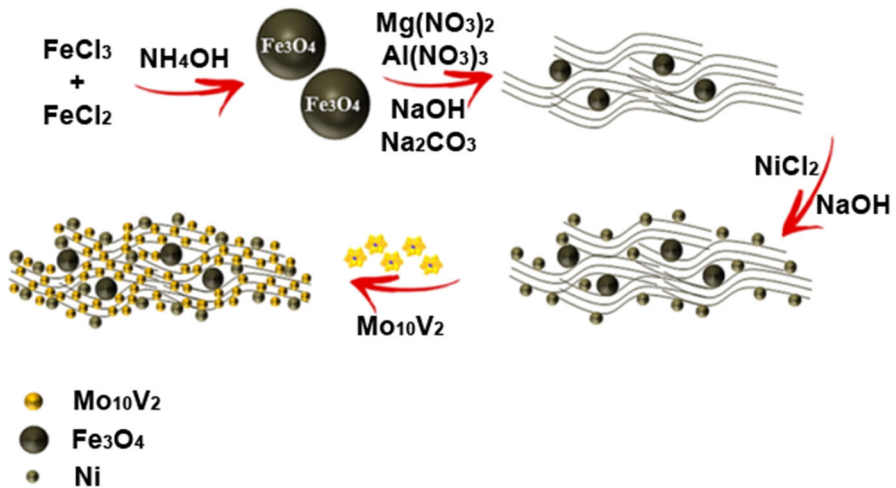
For the Heck coupling reaction, a mixture of aryl halide (4.0 mmol), styrene (4.0 mmol), tetrabutylammonium bromide, TBAB (4.0 mmol), Fe–MgAl/Mo₁₀V₂–Ni (0.03 g) and 5 mL dimethyl formamide (DMF) was charged to the reaction tube. The resulting mixture was refluxed at 120 °C under dry N₂ atmosphere for an appropriate time. The progress of the reaction was monitored by TLC. Upon completion of the reaction, the reaction mixture was then cooled to room temperature and Fe–MgAl/Mo₁₀V₂–Ni was separated by a magnet, washed with diethyl ether (2 × 10 mL), and then dried under vacuum for reuse. The residual mixture was extracted by CH₂Cl₂ (3 × 20 mL), and the combined organic layers were dried over MgSO₄. The solvent was evaporated and the crude products were characterized by ¹H NMR spectroscopy [30].

Results and discussion

In the present work, Fe–MgAl/Mo₁₀V₂–Ni was used as an efficient nano-catalyst in the Heck coupling reaction under base and ligand-free conditions. Simultaneous use of Ni, Mo₁₀V₂ and MgAl LDH in the catalyst structure provides high-surface area bases for Ni nanoparticles, activates the substrates and facilitates the reductive elimination step in the catalytic cycle of the Heck reaction. The synthetic route for the synthesis of the designed heterogeneous catalyst is presented in Scheme 1.

The XRD patterns of Fe₃O₄, Mo₁₀V₂, Fe–MgAl LDH, Fe–MgAl–Ni and Fe–MgAl/Mo₁₀V₂–Ni are presented in Fig. 1. In the XRD pattern of Fe₃O₄ (curve a), all the diffraction peaks can be attributed to cubic-phase Fe₃O₄ {JCPDS-019-0629}. The (220), (311), (400), (422), (511) and (440) reflections of typical Fe₃O₄ indicate the high crystallinity of the Fe₃O₄ nanoparticles. In order to show the presence of Mo₁₀V₂ in our catalyst, the XRD pattern of the Mo₁₀V₂ (curve b) is presented. After addition of MgAl LDH layer to the catalyst structure, the diffraction pattern of the resulting material (curve c) shows sharp absorption reflections for the (003), (006), (105) and (018) planes, which are characteristic of the MgAl LDH structure in addition to the Fe₃O₄ reflections. The sharp and distinctive reflections at 2θ = 11.2° and 23.9° are attributed to the (003) and (006) diffraction planes of MgAl LDHs, respectively.

The XRD pattern of the resulting Fe–MgAl/Mo₁₀V₂–Ni nano-structure (curve e) exhibits the reflections of a Fe₃O₄ and LDH phases. In addition, the curve e, after



Scheme 1 Schematic preparation route of Fe-MgAl/Mo₁₀V₂-Ni

the anion exchange and Ni immobilization processes, shows the presence of Mo₁₀V₂ anions in the MgAl LDH structure, and Ni nanoparticles on the surface of the LDH. The Ni(0) crystals in the catalyst have the crystalline structure with reflections appearing at 44.92°, 51.13° and 76.23° corresponding to the (111), (200) and (220) planes, respectively, of the face-centered cubic structure of the Ni nanoparticles {JCPDS-01-1260}.

The synthesized catalyst possesses a layered structure around the Fe₃O₄ nanoparticles. The layers have an irregular hexagonal morphology which resemble crumpled paper surrounding the magnetic nanoparticles (Fig. 2a). SEM images of the catalyst show the immobilization of Ni nanoparticles on the LDH structures (Fig. 2a, c). The SEM images of Fe-MgAl/Mo₁₀V₂-Ni demonstrated that the presence of LDHs provides a high-surface area structure which plays an important role in the high efficiency and selectivity. Using the EBSD micrograph, the presence of different substances in the catalyst framework was determined. The EBSD image of Fe-MgAl/Mo₁₀V₂-Ni shows the sorted form of Ni(0), Fe₃O₄ and LDH components in the catalyst structure (Fig. 2d). The mapping analysis indicates that the Ni nanoparticles are deposited on the surface of the layered structure of MgAl LDH and that the Fe₃O₄ nanoparticles are distributed throughout the whole LDH structure.

The EDX analysis was also performed to study the elemental composition of the catalyst. The EDX pattern of the catalyst shows major peaks of Mg, Al, Fe, Mo, V and Ni. The results obtained from the EDX analysis confirm the presence of MgAl LDH, Mo₁₀V₂ and Ni nanoparticles in the structure of the synthesized catalyst (Fig. 2m). In agreement with the EDX-elemental analysis of Fe-MgAl/Mo₁₀V₂-Ni, the amount of Ni in the Fe-MgAl/Mo₁₀V₂-Ni structure was 8.28 wt%, which was determined using the ICP-AES measurement. Also, according to the obtained results from ICP-AES measurement, the content of Mo was 15.64 wt%, which indicated that the amount of Mo₁₀V₂ in the Fe-MgAl/Mo₁₀V₂-Ni structure was

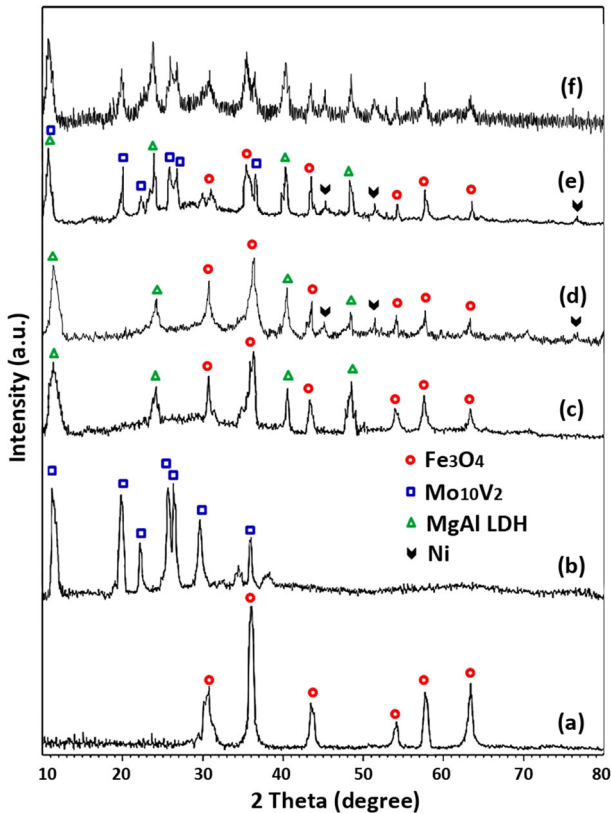


Fig. 1 XRD patterns of: (a) Fe_3O_4 , (b) Mo_{10}V_2 , (c) Fe–MgAl LDH and (d) Fe–MgAl–Ni, (e) Fe–MgAl/ Mo_{10}V_2 –Ni and (f) recovered Fe–MgAl/ Mo_{10}V_2 –Ni

28.32 wt%. The reason for the discrepancy between the obtained results from the EDX-elemental analysis and the ICP-AES measurements is that the EDX-elemental analysis results are based on content evaluation of surface elements, while the ICP-AES technique measures the total amount of molybdenum in the catalyst structure.

For more investigation on the morphology of Fe–MgAl/ Mo_{10}V_2 –Ni, TEM images were recorded and, as expected, clearly confirm the obtained results from the SEM technique (Fig. 3).

The low-magnification image of the layered structure of the catalyst shows dark spots which are attributed to the presence of Ni and Fe_3O_4 nanoparticles in the LDH structure. The high-magnification image clearly reveals the layered structures around the Fe_3O_4 nanoparticles and the distribution of the Ni nanoparticles on the surface of the layers. The Fe_3O_4 and Ni nanoparticles are approximately spherical with diameters below 20 nm.

The FT-IR spectra of Fe_3O_4 , Fe–MgAl LDH, Mo_{10}V_2 and Fe–MgAl/ Mo_{10}V_2 –Ni are presented in Fig. 4. In the FT-IR spectrum of Fe_3O_4 (curve a), the band at 1640 cm^{-1} is attributed to the OH stretching vibration due to the existence of

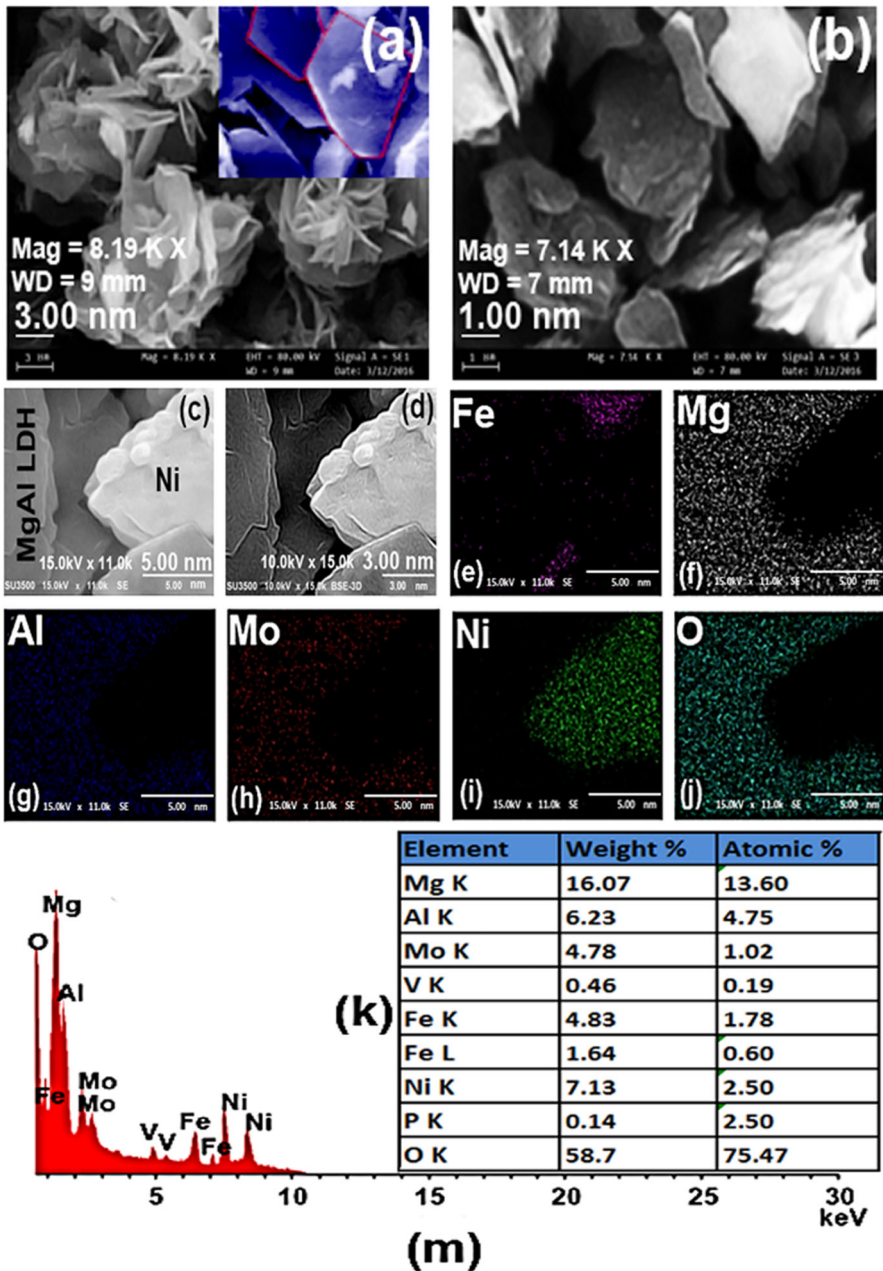


Fig. 2 SEM images of **a, c** fresh Fe-MgAl/Mo₁₀V₂-Ni, **b** recovered Fe-MgAl/Mo₁₀V₂-Ni, **d** EBSD image of Fe-MgAl/Mo₁₀V₂-Ni **e-j** mapping results of Fe-MgAl/Mo₁₀V₂-Ni **k** elemental analysis of Fe-MgAl/Mo₁₀V₂-Ni and **m** EDX results of Fe-MgAl/Mo₁₀V₂-Ni

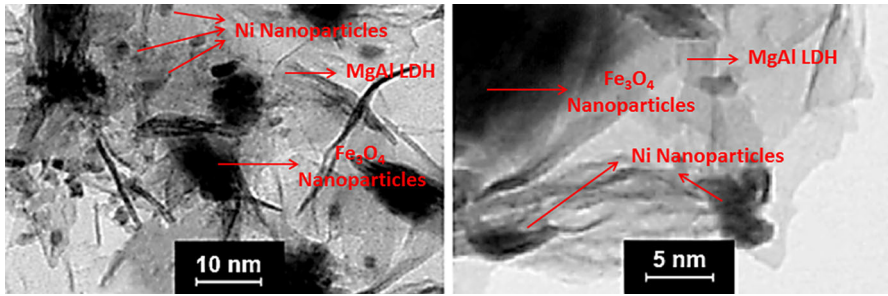
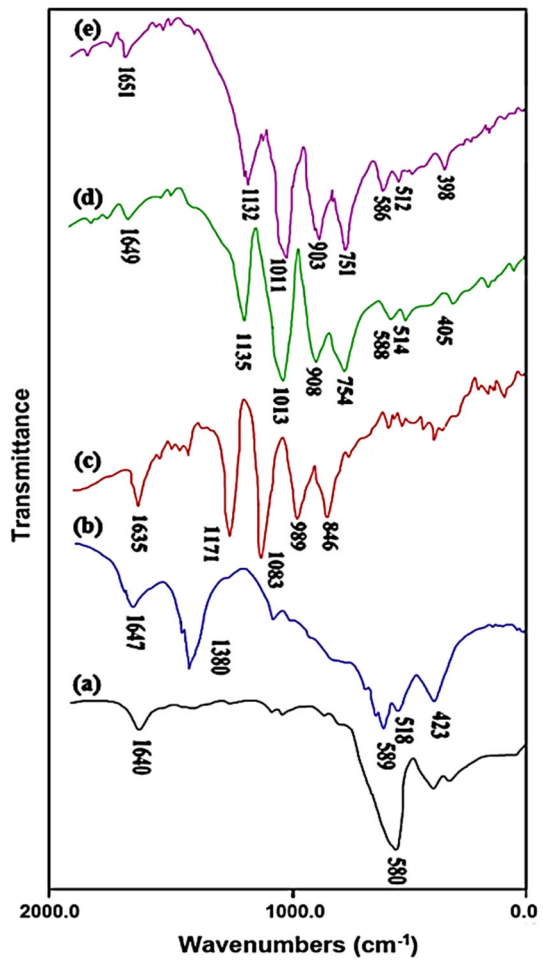


Fig. 3 TEM images of Fe–MgAl/Mo₁₀V₂–Ni

Fig. 4 FT-IR spectra of: (a) Fe₃O₄, (b) Fe–MgAl LDH, (c) Mo₁₀V₂, (d) Fe–MgAl/Mo₁₀V₂–Ni and (e) recovered Fe–MgAl/Mo₁₀V₂–Ni



surface hydroxyl and H_2O . For Fe_3O_4 , Fe–MgAl LDH and Fe–MgAl/ Mo_{10}V_2 –Ni, absorption peaks at about 580 cm^{-1} are ascribed to the Fe–O vibration from the magnetite phase [31]. In the FT-IR spectrum of Fe–MgAl LDH, in addition to Fe_3O_4 characteristic peaks, the absorption bands at 423 and 518 cm^{-1} that are attributed to the M–O vibration modes of LDH structure were observed (curve b). The FT-IR spectra of Fe–MgAl/ Mo_{10}V_2 –Ni, in addition to the Fe_3O_4 peaks at 588 cm^{-1} and LDH characteristic peaks at 405 and 514 cm^{-1} , displays the features of a Keggin-type structure at 1135 , 1013 , 908 and 754 cm^{-1} which are in agreement with the results reported previously (curve d) [22]. Also, the peak at 1380 cm^{-1} due to the carbonate band disappears in the Fe–MgAl/ Mo_{10}V_2 –Ni sample, suggesting that the anion exchange was completed.

In order to investigate the magnetic property of Fe–MgAl/ Mo_{10}V_2 –Ni, a vibrating sample magnetometry (VSM) measurement was performed at 298 K . The magnetization saturated up to 46 emu g^{-1} at an applied field of 8500 Oe reveals the superparamagnetic behavior at room temperature (Fig. 5). This high magnetic property of Fe–MgAl/ Mo_{10}V_2 –Ni facilitates the recovery of the catalyst from the reaction media.

Zeta potentials of Fe–MgAl LDH, Fe–MgAl–Ni and Fe–MgAl/ Mo_{10}V_2 –Ni in the dispersion are positive, and distributed from 26 to 76 (Fe–MgAl LDH), 38 to 81 (Fe–MgAl–Ni) and 13 to 51 mV (Fe–MgAl/ Mo_{10}V_2 –Ni). The average zeta potentials given by the instrument are 57 , 61 and 30 mV for Fe–MgAl LDH, Fe–MgAl–Ni and Fe–MgAl/ Mo_{10}V_2 –Ni, respectively. The positive zeta potential of the LDH structures is in principle attributed to the structural positive charge and the electric double layer on the LDH surface. Although the interior charges of LDHs are fully screened by the interlayer anions, the surface structural charges are not fully balanced by the adsorbed surface anions because the surface-adsorbed anions can desert the electric double layer on the surface of LDHs, and thus the LDH particles have a surface positive charge. In general, since $\text{Mo}_{10}\text{V}_2^{5-}$ is more strongly adsorbed on the surface than CO_3^{2-} and OH^- , and increases the density of the negative charge on the surface, the MgAl LDH and Fe–MgAl–Ni particles show a smaller zeta potential than Fe–MgAl/ Mo_{10}V_2 –Ni. Ni nanoparticles as an electron

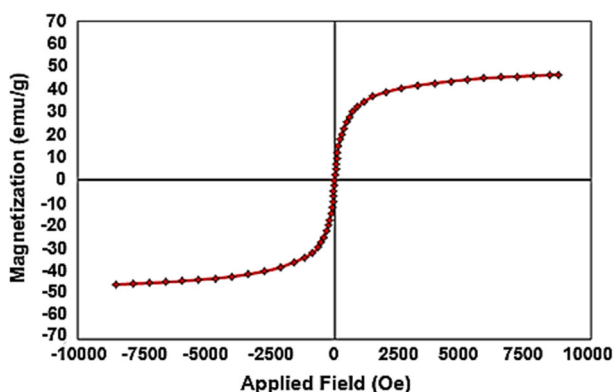


Fig. 5 VSM magnetization curve of Fe–MgAl/ Mo_{10}V_2 –Ni

conductor have a positive surface charge, then, due to the increase of the density of the positive charge on the LDH surfaces, the zeta potential of MgAl LDH particles after deposition of Ni nanoparticles shifted to higher potentials because of the reduction of anions on the surface of the LDHs (Fig. 6).

The surface chemical states of the active sites in Fe–MgAl/Mo₁₀V₂–Ni were investigated using XPS analysis with a typical wide energy scan (Fig. 7). The XPS spectra indicated that the Ni(0), MgAl LDH and Mo₁₀V₂ are present on the surface of Fe–MgAl/Mo₁₀V₂–Ni (Fig. 7a). The MgAl ratio of the catalyst was evaluated from the integral peak area as 2.64, which demonstrates the obtained results from EDX-elemental analysis.

Moreover, the presence of two peaks appearing at 525.1 and 515.7 eV, which are assigned to V_{2p1/2} and V_{2p3/2} and adjunctive ones appearing at 526.9 and 517.1 eV, illustrate the existence of V⁵⁺ and V⁴⁺ species, respectively [32]. Based on the above results, Mo₁₀V₂ can dramatically affect the charge state of Ni nanoparticles, promoting the formation of V⁴⁺ and Ni²⁺ species, which is a beneficial species to catalyze the oxidation reactions (Fig. 7b). Also, there are two peaks at 853.2 and 869.8 eV which correspond to Ni_{2p1/2} and Ni_{2p3/2} accompanied by two weak peaks at 858.7 and 873.7 eV belonging to Ni^{II}_{2p1/2} and Ni^{II}_{2p3/2}, respectively (Fig. 7c). According to the obtained results from these analyses, there is a small amount of Ni²⁺ on the surface of this catalyst, which could be caused by the electron transfer between Ni(0) and Mo₁₀V₂ or the formation of Ni–O species. A 0.5-eV shift to higher binding energy with respect to the neutral form of Ni(0) for the Fe–MgAl/Mo₁₀V₂–Ni indicates a decrease in the electron density of Ni(0), which confirms the electron transfer from Ni(0) to Mo₁₀V₂ species. Also, the appearance of peaks at 711.1 and 724.2 eV show the Fe₃O₄ nanoparticles on the surface of the catalyst. It has been previously reported that Fe_{2p3/2} for Fe₃O₄ does not have a satellite peak [33, 34], and this absence has been confirmed in the present study (Fig. 7d).

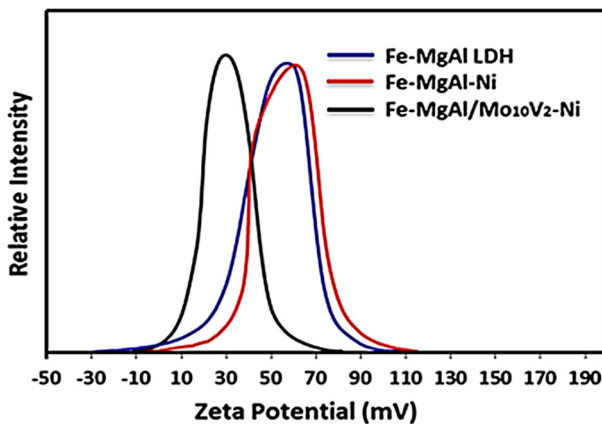


Fig. 6 Zeta potential distribution of Fe–MgAl LDH, Fe–MgAl–Ni and Fe–MgAl/Mo₁₀V₂–Ni nanoparticles

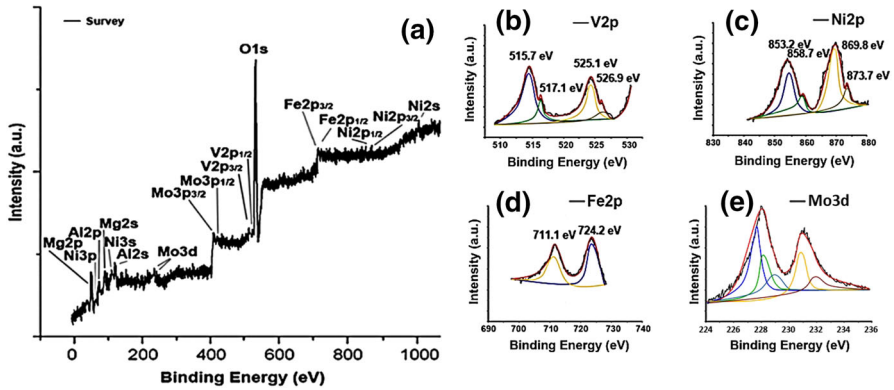


Fig. 7 XPS analysis of a Fe-MgAl/Mo₁₀V₂-Ni with wide energy scan; high-resolution XPS spectra of **b** 2*p* region of V, **c** 2*p* region of Ni, **d** 2*p* region of Fe and **e** 3*d* region of Mo

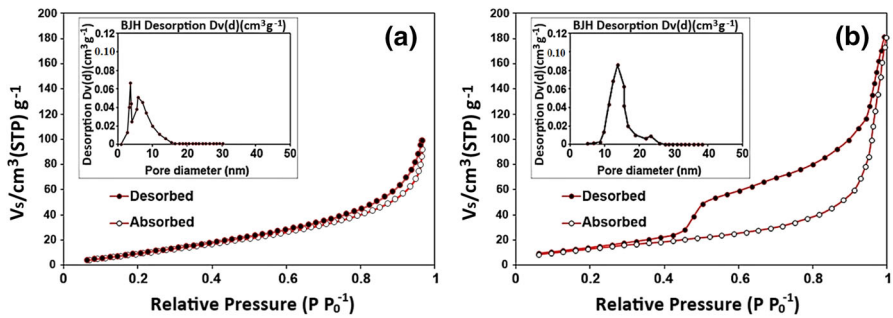


Fig. 8 Isotherm and pore distribution curves of **a** Fe-MgAl-Ni and **b** Fe-MgAl/Mo₁₀V₂-Ni, based on the BET and BJH methods, respectively

The physical surface features of Fe-MgAl-Ni and Fe-MgAl/Mo₁₀V₂-Ni were investigated using the N₂ adsorption-desorption isotherm and the related pore distribution curves (Fig. 8). Both of the mentioned structures show a type IV isotherm related to the mesoporous materials which indicates the presence of nano-voids in the Fe-MgAl-Ni and Fe-MgAl/Mo₁₀V₂-Ni structures. It was observed that the presence of Mo₁₀V₂ in the Fe-MgAl/Mo₁₀V₂-Ni structure significantly increases the surface area. The corresponding specific surface areas of Fe-MgAl-Ni and Fe-MgAl/Mo₁₀V₂-Ni are about 6.44 and 87.5 m² g⁻¹, respectively.

Also, BJH pore size distribution of Fe-MgAl/Mo₁₀V₂-Ni exhibit a narrow mesopore size distribution centered at 13.7 nm which is higher than Fe-MgAl-Ni (7.6 nm). The pore volumes of Fe-MgAl-Ni and Fe-MgAl/Mo₁₀V₂-Ni were measured at about 0.073 and 0.256 cm³ g⁻¹, respectively, by BJH analysis. Fe-MgAl/Mo₁₀V₂-Ni indicates high BET surface area with the large pore volume superior to most of the reported porous POM hybrids paired with organic or inorganic parts (e.g., triammonium cations) [35], ionic liquids [36, 37], and zinc phosphate [38, 39], even surpassing poly(ionic liquid)-supported POMs [40] and

comparable to the specific surface areas ($85\text{--}156\text{ m}^2\text{ g}^{-1}$) for the conventional micro/mesoporous NH_4^+ and Cs^+ salts of POMs [41].

In order to show the structural stability of the catalyst, TGA has been performed on Fe–MgAl/Mo₁₀V₂–Ni (Fig. 9). Three mass loss steps occurred with an increase of the temperature. The first mass loss step in the range of 30–280 °C is ascribed to the elimination of water molecules absorbed on the surface and interlayer space of Fe–MgAl/Mo₁₀V₂–Ni (11.45 wt%). This step is composed of simultaneous elimination of crystalline and participant water. The second mass loss step at 280–480 °C is attributed to lamellar hydroxyl group loss (dehydroxylation) as well as anions loss (6.94 wt%). Also, partial mass gain in the range of 480–540 °C indicated that Ni nanoparticles begin to be oxidized into metal oxides. The third mass loss of 2.30 wt% at 540–1000 °C corresponds to decomposition of the Mo₁₀V₂ anions [42].

The electrocatalytic behaviors of Fe–MgAl–Ni, Mo₁₀V₂ and Fe–MgAl/Mo₁₀V₂–Ni were investigated in 0.1 M PBS by cyclic voltammetry (CV). According to the obtained results from the comparison of the cyclic curves of Fe–MgAl–Ni and Fe–MgAl/Mo₁₀V₂–Ni, the presence of Mo₁₀V₂ not only significantly enhanced the oxidation peak current of Fe–MgAl–Ni but also decreased its oxidation peak potential from 0.41 to 0.39 V, suggesting that the electrochemical oxidation strength of Fe–MgAl–Ni was increased by the presence of Mo₁₀V₂ after the anion exchange process (Fig. 10). Also, the transfer of electrons from Ni(0) to Mo₁₀V₂ significantly enhanced the oxidation peak current of Fe–MgAl–Ni. The increase in the oxidation peak current of Fe–MgAl–Ni shows the increment of the concentration of electroactive Ni species at the electrode–solution interface which are generated by the presence of Mo₁₀V₂.

The linear sweep voltammetry (LSV) curves of Fe–MgAl LDH, Fe–MgAl–Ni and Fe–MgAl/Mo₁₀V₂–Ni are presented in Fig. 11a. The onset potentials were measured to be 424.83, 416.22 and 398.73 mV for Fe–MgAl LDH, Fe–MgAl–Ni

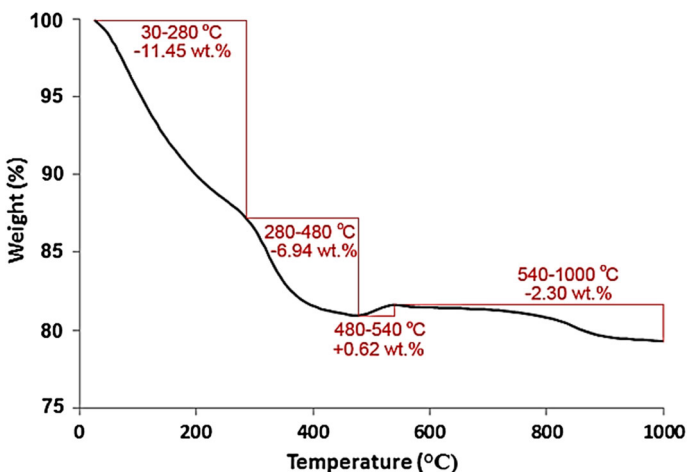


Fig. 9 TGA curve of Fe–MgAl/Mo₁₀V₂–Ni

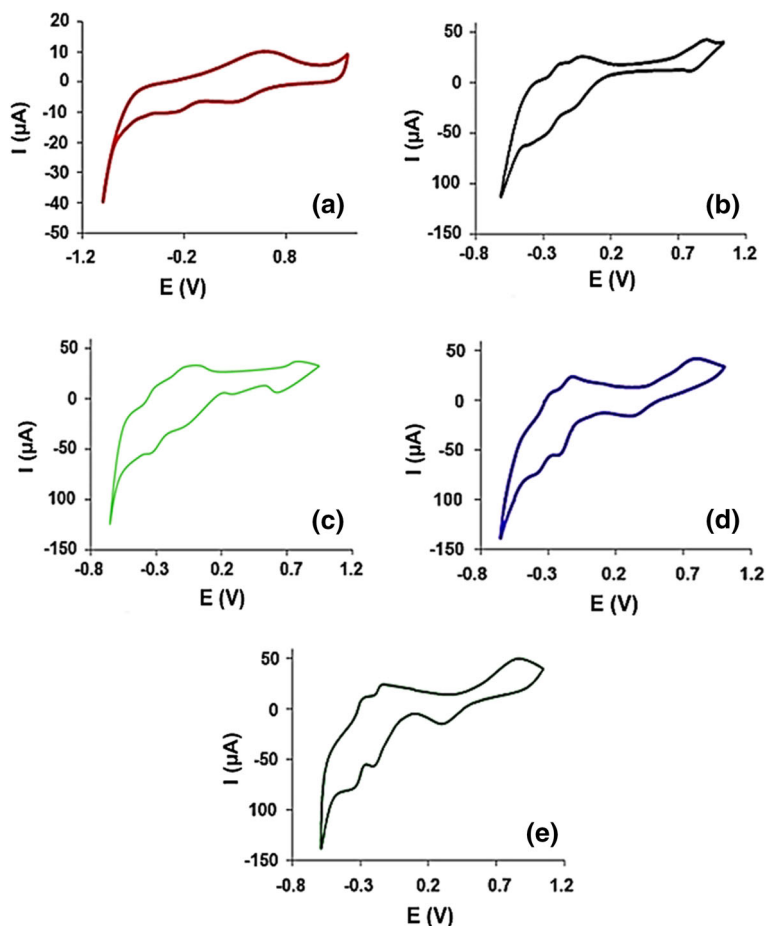


Fig. 10 Cyclic voltammograms of **a** Fe–MgAl–Ni, **b** Mo₁₀V₂, **c** Fe–MgAl/Mo₁₀V₂ **d** Fe–MgAl/Mo₁₀V₂–Ni and **e** recovered Fe–MgAl/Mo₁₀V₂–Ni CPE in PBS, 100 mV s^{−1}

and Fe–MgAl/Mo₁₀V₂–Ni, respectively. The comparison of these LSV curves reveals that the Fe–MgAl/Mo₁₀V₂–Ni shows lower onset potential and higher limited current density. On the basis of the obtained data from the electrocatalytic experiments, it can be shown that the electron transfer between Mo₁₀V₂ and Ni species greatly helps to enhance the electrocatalytic activity of Fe–MgAl–Ni in the Heck coupling reactions.

The improvement in catalytic kinetic of the catalyst is also comparably investigated using Tafel slopes (Fig. 11b). Fe–MgAl/Mo₁₀V₂–Ni offers a lower Tafel slope of 51 mV dec^{−1}, smaller than those of Fe–MgAl–Ni (59 mV dec^{−1}) and Fe–MgAl LDH (63 mV dec^{−1}). This smaller Tafel slope value for the Fe–MgAl/Mo₁₀V₂–Ni catalyst results in a further enhancement toward catalytic activity. In other words, the lowered Tafel slope indicates that electron transfer

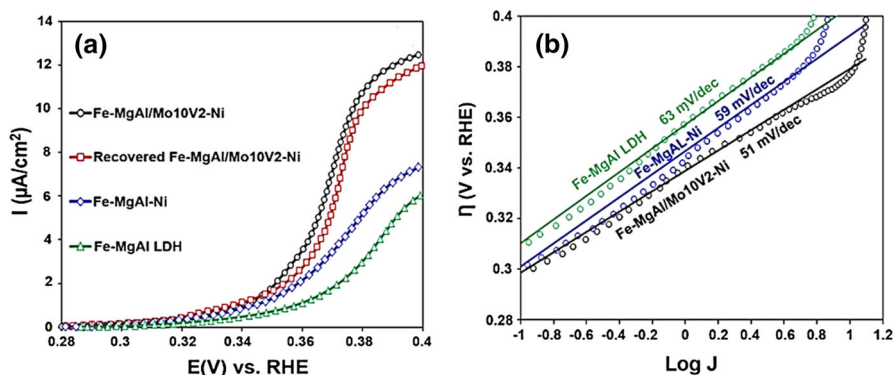


Fig. 11 a LSV curves of Fe–MgAl LDH, Fe–MgAl–Ni, Fe–MgAl/Mo₁₀V₂–Ni and recovered Fe–MgAl/Mo₁₀V₂–Ni, recorded at in PBS, 100 mV s⁻¹, b Tafel plots of Fe–MgAl–Ni and Fe–MgAl/Mo₁₀V₂–Ni derived from the corresponding LSV curves

becomes more achievable on Fe–MgAl/Mo₁₀V₂–Ni compared with Fe–MgAl LDH or Fe–MgAl–Ni.

Electrochemical active surface area (ECSA) is a valuable factor for catalysts in electrochemical reactions. Increase of ECSA of the catalyst often leads to enhancement of the catalytic activity. In order to probe the ECSA of Fe–MgAl/Mo₁₀V₂–Ni, the LSV curves of the catalyst, Fe–MgAl–Ni and Fe–MgAl LDH in PBS under different scan rates were investigated. By plotting the limiting current in the LSV curves of Fe–MgAl/Mo₁₀V₂–Ni and Fe–MgAl–Ni against the scan rate, the linear slope can be used to represent the attributed ECSA.

The ECSA of Fe–MgAl/Mo₁₀V₂–Ni is 6.16, while Fe–MgAl–Ni and Fe–MgAl LDH have lower linear slopes, which indicate that the presence of Mo₁₀V₂ in the

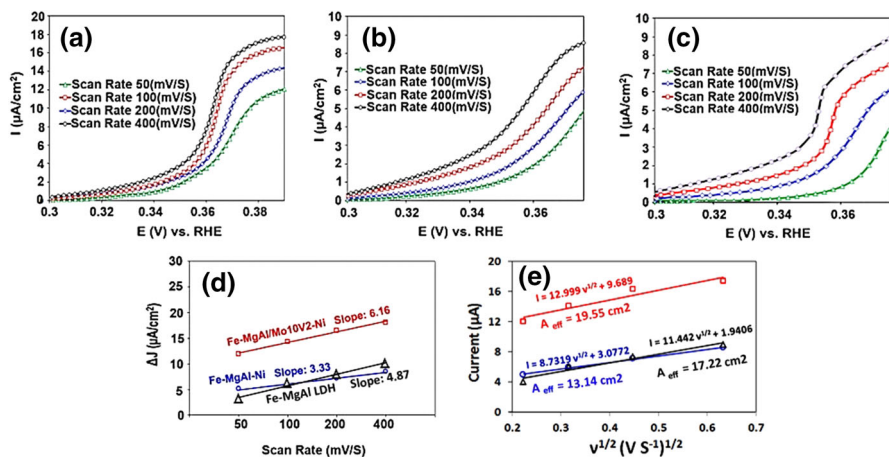


Fig. 12 LSV curves of a Fe–MgAl/Mo₁₀V₂–Ni, b Fe–MgAl–Ni, and c Fe–MgAl LDH in PBS under different scan rates, d the limiting current against the scan rate, and e the relationship between the peak current and the square root of the scan rate fitted by the Randles–Sevcik equation

catalyst structure, in addition to the improvement of the electrocatalytic behavior of the catalyst, provides higher electroactive surface centers in the catalyst structure (Fig. 12d). Also, the effective area of the Fe–MgAl/Mo₁₀V₂–Ni, Fe–MgAl–Ni and Fe–MgAl LDH ($A_{\text{eff}} \text{ cm}^2$) were estimated by the Randles–Sevcik equation:

$$I_{\text{pa}} = (2.69 \times 10^5) n^{2/3} A_{\text{eff}} D^{1/2} v^{1/2} C_0$$

where D and C_0 are the diffusion coefficient and bulk concentration of the redox probe, respectively. The other symbols have their usual meanings. LSV experiments under different scan rates were performed with the Fe–MgAl/Mo₁₀V₂–Ni, Fe–MgAl–Ni and Fe–MgAl LDH CPE immersed in PBS. In the range of the scan rate, the current varies linearly with the square root of the scan rate. Here, the slope of Randles–Sevcik plots is proportional to the active surface area (Fig. 12e).

In the next step of our investigation, the catalytic activity of Fe–MgAl/Mo₁₀V₂–Ni in the Heck coupling reactions was evaluated. In order to probe the best reaction conditions, the reaction of bromobenzene (4 mmol) and styrene (4 mmol) in the presence of tetrabutylammonium bromide (TBAB) at 120 °C under ligand and base-free conditions was chosen as a model reaction.

In the absence of the catalyst, the reaction did not proceed at all and the starting materials remained intact after 24 h (Table 1, entry 1). To establish the best reaction conditions, the effects of various solvents, such as H₂O, dimethyl acetamide (DMAc) and DMF, have been studied (Table 1, entries 2–4). DMF at 120 °C was found to be the choice in terms of the efficiency of the reaction (entry 2). Next, the amount of Fe–MgAl/Mo₁₀V₂–Ni was examined, and it seems that 0.03 g of Fe–MgAl/Mo₁₀V₂–Ni was sufficient to drive the reaction in 86% yield. Using less Fe–MgAl/Mo₁₀V₂–Ni led to a lower yield even with extended reaction time. Also, further increasing the catalyst quantity showed no significant improvement in the yield or reaction time. Therefore, 0.03 g of the catalyst was chosen as the optimum amount of Fe–MgAl/Mo₁₀V₂–Ni for further reactions.

The scope and generality of use of Fe–MgAl/Mo₁₀V₂–Ni were explored with respect to various aryl halides and styrene. All products were obtained in good to excellent yields under the optimized conditions (Table 2).

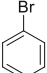
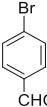
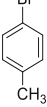
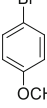
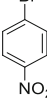
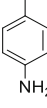
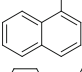
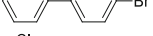
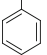
Table 1 Optimization of Heck coupling reaction conditions

| Entry | Fe–MgAl/Mo ₁₀ V ₂ –Ni (g) | Solvent | Yield (%) ^a |
|-------|---|------------------|------------------------|
| 1 | – | DMF | – |
| 2 | 0.01 g | DMF | 63 |
| 3 | 0.01 g | H ₂ O | 8 |
| 4 | 0.01 g | DMAc | 39 |
| 5 | 0.02 g | DMF | 71 |
| 6 | 0.03 g | DMF | 86 |
| 7 | 0.04 g | DMF | 88 |

Reaction conditions: styrene (4 mmol), bromobenzene (4 mmol), TBAB (4 mmol), 24 h and at 120 °C

^aIsolated yield

Table 2 Heck reaction of various aryl halides with styrene

| Entry | Aryl halide | Time (h) | Yield (%) ^{a, b} |
|-------|---|----------|---------------------------|
| 1 |  | 9 | 86 |
| 2 |  | 8 | 92 |
| 3 |  | 12 | 74 |
| 4 |  | 12 | 71 |
| 5 |  | 8 | 93 |
| 6 |  | 16 | 68 |
| 7 |  | 9 | 86 |
| 8 |  | 12 | 79 |
| 9 |  | 24 | 56 |

Reaction conditions: styrene (4 mmol), aryl halide (4 mmol), TBAB (4 mmol) at 120 °C

^aIsolated yield

^bIdentification of the products was ascertained by NMR analysis

According to the obtained results from Table 2, each aryl halide containing electron-withdrawing or electron-releasing groups reacts efficiently with styrene for the generation of the corresponding products. Electronic effects on the aromatic ring of aryl halides have a significant influence on the reaction efficiency. Those containing electron-withdrawing groups give the desired products in higher yields (entries 2 and 5), but aryl halides bearing electron-releasing groups give the targets in comparatively lower yields (entries 3, 4 and 6). To our surprise, condensation of chlorobenzene with styrene affords the respective product in a moderate yield (entry 9).

Reusability of Fe–MgAl/Mo₁₀V₂–Ni makes the Heck coupling reaction more economical. After each run, the catalyst was separated using an external magnet, washed with a suitable solvent and dried, as described in the “[Experimental](#)” section. The catalyst revealed a remarkable activity and was reused up to at least four consecutive cycles without a measurable reduction in the catalytic activity of the catalyst. In the fourth reaction run of the model reaction, the yield of the products decreased from 86 (yield of the first run) to 78% (Fig. 13).

Recyclability of the Fe–MgAl/Mo₁₀V₂–Ni was evaluated under the optimized conditions shown in Table 2. At the end of the fourth reaction run, 90 wt% of the catalyst (compared with the amount of the fresh catalyst used in the first run) was recovered (Fig. 13). In addition, the structural variations of Fe–MgAl/Mo₁₀V₂–Ni after the recovery process were investigated using XRD, SEM and FT-IR techniques. According to the obtained results, the structural features of the catalyst were retained after reuse (Figs. 1e, 2b, 4e). Also, the electrochemical behavior of the catalyst after the first run was probed using CV and LSV measurements. The cyclic and linear sweep voltammograms of the recovered Fe–MgAl/Mo₁₀V₂–Ni showed no significant changes in electrocatalytic properties (Figs. 10d, 11a).

A plausible mechanism for the Heck coupling reaction catalyzed by Fe–MgAl/Mo₁₀V₂–Ni is proposed in Scheme 2. In a first step, the C–X bond activation of an aryl halide (X = Br, Cl) affected by Mo₁₀V₂ occurs and then is oxidatively added to the Ni atoms. Next, Ni forms a π complex with the alkene, and then the alkene insertion in the Ni–Ar bond takes place. In continuance, a new Ni–alkene π complex forms in a β -hydride elimination step. Finally, this complex is destroyed and the desired product released. Also, the Ni(0) species regenerates by reductive elimination of the Ni(II) compound using the electron transfer ability of Mo₁₀V₂ species. In this step, the elimination of HX from the Ni(II) facilitates the proton affinity of Mo₁₀V₂ ions.

According to the electrochemical results, the presence of Mo₁₀V₂ facilitates the electron transfer ability of nickel in the catalytic cycle, both in oxidative addition and reductive elimination steps. Addenda metals in POMs are present in their

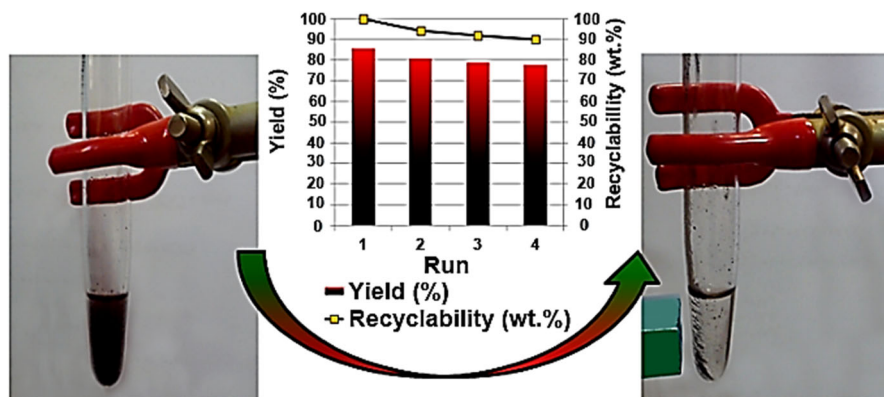
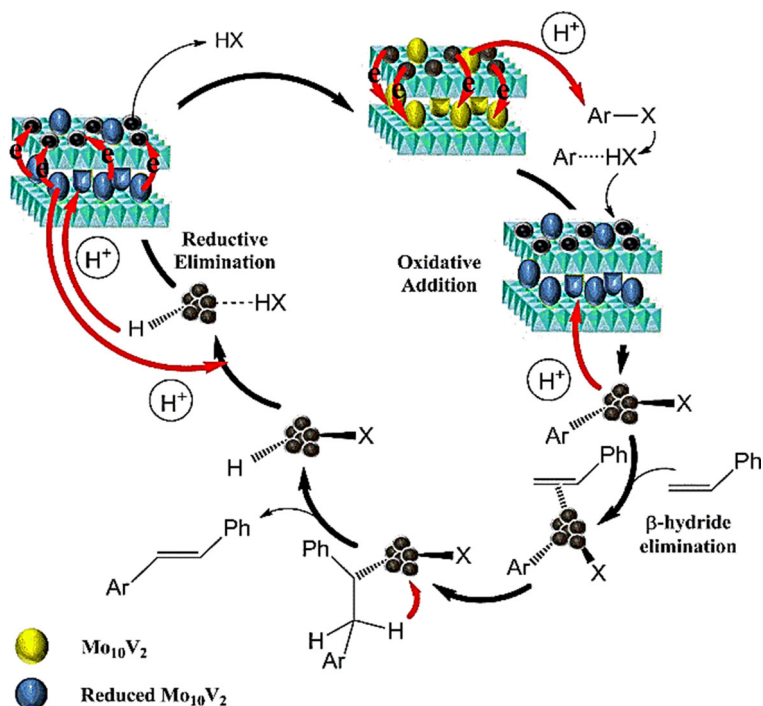


Fig. 13 Reusability of Fe–MgAl/Mo₁₀V₂–Ni in the model reaction after 24 h reaction time and catalyst recovery process



Scheme 2 Proposed mechanism for the Heck reaction catalyzed by Fe–MgAl/Mo₁₀V₂–Ni

highest oxidation state, typically in d^0 or d^1 electronic configurations. Thus, metal centers are willing to accept external electrons because of their empty valence shell. Fully oxidized addenda atoms usually have formal charges between + 4 and + 6. This number could vary by the state of reduction of the molecules. Even though they are negatively charged, reductions are common. The low-lying empty d -type orbitals of the addenda atoms can accept numerous electrons with no major changes in their geometry. These extra electrons, located in d -metal orbitals, are called blue electrons (Scheme 2, reduced Mo₁₀V₂). This phenomenon is easier in POMs containing Mo and/or V compared with W ones, because these ions are easily reduced [43]. Further research is under investigation in our laboratory.

Conclusion

In the present study, the first example of Ni immobilized on an Fe–MgAl LDH structure with Mo₁₀V₂ anions for use as an efficient and recyclable catalyst in the Heck coupling reaction has been reported. The key tool to maximize the performance of this catalyst is the use of Mo₁₀V₂ in the LDH structure. The presence of Mo₁₀V₂ is essential for obtaining high performance of the catalyst; most probably, it can activate precursors of the reaction and facilitate transfer of the electrons to or from the Ni species in the catalytic cycle. Characterization of the

prepared catalyst was investigated by FT-IR, XRD, ICP-AES, TEM, SEM, EDX, EBSD, XPS, BET, VSM, CV, LSV and zeta potential techniques. LSV and CV show a synergic effect between Mo_{10}V_2 and nickel nanoparticles. Increasing of ECSA of the catalyst compared to the Fe–Mg–Al–Ni leads to enhancement of the catalytic activity and proves the synergic effect. Investigation of the magnetic properties of the catalyst exhibits superparamagnetic behavior, which suggests that Fe–MgAl/Mo₁₀V₂–Ni can easily recover from the reaction media. In addition, the structure, catalytic activity and electrochemical behavior of the catalyst after the reaction was probed using SEM, XRD, FT-IR, CV and LSV analyses and were retained unchanged. Further studies on extending the application of this type of catalytic system in coupling reactions are ongoing in our laboratory.

Acknowledgement The authors thank the Razi University Research Council and Iran National Science Foundation (INSF) for support of this work.

References

1. R.F. Heck, J. Nolley Jr, *J. Org. Chem.* **37**, 2320 (1972)
2. I.P. Beletskaya, A.V. Cheprakov, *Chem. Rev.* **100**, 3009 (2000)
3. W.A. Herrmann, C. Brossmer, K. Öfele, C.P. Reisinger, T. Priemermeier, M. Beller, H. Fischer, *Angew. Chem. Int. Ed. Eng.* **34**, 1844 (1995)
4. J. Mo, L. Xu, J. Ruan, S. Liu, J. Xiao, *Chem. Commun.* **34**, 3591 (2006)
5. I.P. Beletskaya, A.V. Cheprakov, in *Handbook of Organopalladium Chemistry for Organic Synthesis*, (John Wiley & Sons, Inc., Hoboken, United Stat of America, 2002), p. 2955. <https://doi.org/10.1002/0471212466.ch143>.
6. M. Oestreich, *The Mizoroki-Heck Reaction* (Wiley, New York, 2009)
7. B.-L. Lin, L. Liu, Y. Fu, S.-W. Luo, Q. Chen, Q.-X. Guo, *Organometallics* **23**, 2114 (2004)
8. N. Nowrouzi, M. Zarei, *Tetrahedron* **71**, 7847 (2015)
9. A. Houdayer, R. Schneider, D. Billaud, J. Ghanbaja, J. Lambert, *Synth. Met.* **151**, 165 (2005)
10. S. Ma, H. Wang, K. Gao, F. Zhao, *J. Mol. Catal. A Chem.* **248**, 17 (2006)
11. B.H. Lipshutz, S. Tasler, W. Chrisman, B. Spliethoff, B. Tesche, *J. Org. Chem.* **68**, 1177 (2003)
12. B.M. Bhanage, F. Zhao, M. Shirai, M. Arai, *Catal. Lett.* **54**, 195 (1998)
13. J. Han, Y. Dou, M. Wei, D.G. Evans, X. Duan, *Angew. Chem. Int. Ed.* **49**, 2171 (2010)
14. S. Miyata, *Clays Clay Miner.* **31**, 305 (1983)
15. P. Dutta, M. Puri, *Phys. Chem.* **93**, 376 (1989)
16. L.M. Parker, N.B. Milestone, R.H. Newman, *Ind. Eng. Chem. Res.* **34**, 1196 (1995)
17. F. Cavani, F. Trifirò, A. Vaccari, *Catal. Today* **11**, 173 (1991)
18. H. Zhang, R. Qi, D.G. Evans, X. Duan, *J. Solid State Chem.* **177**, 772 (2004)
19. L. Li, Y. Feng, Y. Li, W. Zhao, J. Shi, *Angew. Chem.* **121**, 6002 (2009)
20. Y. Guo, D. Li, C. Hu, Y. Wang, E. Wang, *Int. J. Inorg. Mater.* **3**, 347 (2001)
21. Y. Watanabe, K. Yamamoto, T. Tatsumi, *J. Mol. Catal. A Chem.* **145**, 281 (1999)
22. E. Rafiee, M. Kahrizi, *J. Mol. Liq.* **218**, 625 (2016)
23. E. Rafiee, M. Kahrizi, *Res. Chem. Intermed.* **42**, 1125 (2016)
24. E. Rafiee, M. Kahrizi, M. Joshaghani, P.G.-S. Abadi, *Res. Chem. Intermed.* **42**, 5573 (2016)
25. V. Kogan, Z. Aizenshtat, R. Popovitz-Biro, R. Neumann, *Org. Lett.* **4**, 3529 (2002)
26. A. Corma, S. Iborra, F. Llabres i Xamena, R. Monton, J. Calvino, C. Prestipino, *J. Phys. Chem. C* **114**, 8828 (2010)
27. S. Berardi, M. Carraro, M. Iglesias, A. Sartorel, G. Scorrano, M. Albrecht, M. Bonchio, *Chem. Eur. J.* **16**, 10662 (2010)
28. M.M. Lorian, B. Matt, S. Alves, A. Proust, G. Poli, J. Oble, G. Izzet, *Chem. Eur. J.* **19**, 12607 (2013)
29. E. Rafiee, M. Kahrizi, *Res. Chem. Intermed.* **43**, 6665 (2017)
30. E. Rafiee, A. Ataei, S. Nadri, M. Joshaghani, S. Eavani, *Inorg. Chim. Acta* **409**, 302 (2014)

31. M. Yamaura, R. Camilo, L. Sampaio, M. Macedo, M. Nakamura, H. Toma, J. Magn. Mater. **279**, 210 (2004)
32. G. Chen, Y. Zhou, X. Wang, J. Li, S. Xue, Y. Liu, Q. Wang, J. Wang, *Sci. Rep.* **5**, 11236 (2015)
33. M. Muhler, R. Schlögl, G. Ertl, *J. Catal.* **138**, 413 (1992)
34. D.D. Hawn, B.M. DeKoven, *Surf. Interface Anal.* **10**, 63 (1987)
35. M.V. Vasylyev, R. Neumann, *J. Am. Chem. Soc.* **126**, 884 (2004)
36. G. Chen, Y. Zhou, P. Zhao, Z. Long, J. Wang, *ChemPlusChem* **78**, 561 (2013)
37. G. Chen, Y. Zhou, Z. Long, X. Wang, J. Li, J. Wang, *A.C.S. Appl. Mater. Interfaces* **6**, 4438 (2014)
38. S. Uchida, S. Hikichi, T. Akatsuka, T. Tanaka, R. Kawamoto, A. Lesbani, Y. Nakagawa, K. Uehara, N. Mizuno, *Chem. Mater.* **19**, 4694 (2007)
39. A.C. Kalita, C. Roch-Marchal, R. Murugavel, *Dalton Trans.* **42**, 9755 (2013)
40. C. Gao, G. Chen, X. Wang, J. Li, Y. Zhou, J. Wang, *Chem. Commun.* **51**, 4969 (2015)
41. K. Inumaru, *Catal. Surv. Asia* **10**, 151 (2006)
42. Y. Jia, S. Zhao, Y.-F. Song, *Appl. Catal. A Gen.* **487**, 172 (2014)
43. I.K. Song, M.A. Barteau, *J. Mol. Catal. A Chem.* **212**, 229 (2004)